

# Multi-Frequency Multi-Resolution Stochastic Optimization for GPR Microwave Imaging

M. Salucci, L. Poli, N. Anselmi, and A. Massa

## Abstract

In this work, the retrieval of the dielectric characteristics of unknown objects buried in a lossy half-space is dealt with. An innovative multi-resolution multi-frequency (*MF*) stochastic microwave imaging technique is proposed to solve the buried inverse scattering problem by processing wide-band ground penetrating radar (*GPR*) data. The proposed *MF-IMSA-PSO* method exploits a particle swarm optimization (*PSO*)-based algorithm to find the global optimum of the *MF* cost function measuring the mismatch between available and retrieved data at a fixed set of frequencies. Such a stochastic solver is nested within the iterative multi-scaling approach (*IMSA*) in order to reduce the ratio between problem unknowns and informative data, as well as to adaptively enforce increasing resolutions only within the regions of interest in which the scatterers have been detected. A preliminary numerical validation is shown, in order to assess the robustness of the developed approach with respect to noise, as well as to compare its performance to state-of-the-art competitive approaches.

# 1 Definitions

## 1.1 Glossary

- $SF$ : Single-Frequency;
- $FH$ : Frequency-Hopping;
- $MF$ : Multi-Frequency;
- $P$ : Swarm dimension;
- $U$ : Total number of unknowns;
- $S$ : Maximum number of  $IMSA$  zooming steps;
- $s^{best}$ : Last performed  $IMSA$  zooming step ( $s^{best} \leq S$ );
- $\eta_{th}$ :  $IMSA$  zooming threshold;
- $D_{inv}$ : Investigation domain;
- $D_{obs}$ : Observation domain;
- $L$ : Side of the investigation domain;
- $N$ : Number of discretization cells in  $D_{ind}$ ;
- $V$ : Number of views;
- $M$ : Number of measurement points;
- $F$ : Number of frequencies considered for the inversion;
- $\mathbf{r}^{(v)} = (x^{(v)}, y^{(v)})$ : Coordinates of the  $v$ -th source ( $v = 1, \dots, V$ ).
- $\mathbf{r}_m^{(v)} = (x_m^{(v)}, y_m^{(v)})$ : Coordinates of the  $m$ -th measurement point for the  $v$ -th view  $v$ , ( $m = 1, \dots, M$ );
- $\varepsilon_{ra} = \frac{\varepsilon_a}{\varepsilon_0}$ : Relative electric permittivity for the upper half-space ( $y > 0$ );
- $\sigma_a$ : Conductivity for the upper half-space ( $y > 0$ );
- $\varepsilon_{rb} = \frac{\varepsilon_b}{\varepsilon_0}$ : Background relative electric permittivity;
- $\sigma_b$ : Background conductivity;
- $E_{inc}^{(v)}(\mathbf{r}_n; f)$ : Measured internal incident field inside the  $n$ -th cell, for the  $v$ -th view at frequency  $f$ ;
- $\tilde{E}_{inc}^{(v)}(\mathbf{r}_n; f)$ : Computed internal incident field inside the  $n$ -th cell, for the  $v$ -th view at frequency  $f$ ;
- $E_{scatt}^{(v)}(\mathbf{r}_m^{(v)}; f)$ : Measured external scattered by the  $m$ -th measurement point, for the  $v$ -th view at frequency  $f$ ;
- $\tilde{E}_{scatt}^{(v)}(\mathbf{r}_m^{(v)}; f)$ : Measured external scattered by the  $m$ -th measurement point, for the  $v$ -th view at frequency  $f$ .

## 1.2 Contrast function

The contrast function at frequency  $f$  is defined as

$$\tau(\mathbf{r}; f) = \frac{\varepsilon_{eq}(\mathbf{r}) - \varepsilon_{eqb}}{\varepsilon_0} = [\varepsilon_r(\mathbf{r}) - \varepsilon_{rb}] + j \left[ \frac{\sigma_b - \sigma(\mathbf{r})}{2\pi f \varepsilon_0} \right]$$

where

- $\mathbf{r} = (x, y)$ : position vector;
- $\Re\{\tau(\mathbf{r}; f)\} = [\varepsilon_r(\mathbf{r}) - \varepsilon_{rb}]$  ;
- $\Im\{\tau(\mathbf{r}; f)\} = \left[ \frac{\sigma_b - \sigma(\mathbf{r})}{2\pi f \varepsilon_0} \right]$ ;
- $\varepsilon_{eq}(\mathbf{r}) = \varepsilon_0 \varepsilon_r(\mathbf{r}) - j \frac{\sigma(\mathbf{r})}{2\pi f}$  ;
- $\varepsilon_{eqb} = \varepsilon_0 \varepsilon_{rb} - j \frac{\sigma_b}{2\pi f}$ ;
- $\varepsilon_r(\mathbf{r})$ : relative electric permittivity at position  $\mathbf{r}$ ;
- $\sigma(\mathbf{r})$ : conductivity at position  $\mathbf{r}$ ;

**NOTE:** we assume that  $\varepsilon_r(\mathbf{r})$  and  $\sigma(\mathbf{r})$  are **not frequency dependent** (non-dispersive mediums).

### 1.2.1 Contrast function and reference frequency $f_{ref}$ (MF approaches)

The contrast function at a generic frequency  $f$  can be expressed by means of the contrast function computed for a selected reference frequency

$$f = f_{ref} \tag{1}$$

as follows

$$\tau(\mathbf{r}; f) = \Re\{\tau(\mathbf{r}; f_{ref})\} + j \frac{f_{ref}}{f} \Im\{\tau(\mathbf{r}; f_{ref})\}. \tag{2}$$

This allows to reduce the number of unknowns when dealing with multi-frequency techniques, since we can just consider the contrast function at the reference frequency.

### 1.3 Cost function & unknowns

#### 1.3.1 Multi-Frequency (*MF*) approaches

These approaches jointly consider data at  $F$  frequencies. The functional minimized by the inversion algorithm is defined as

$$\Phi(\mathbf{x}) = \Phi_{state}(\mathbf{x}) + \Phi_{data}(\mathbf{x}) \quad (3)$$

where  $\Phi_{state}(\mathbf{x})$  and  $\Phi_{data}(\mathbf{x})$  are respectively the data and state terms of the cost function, defined as

$$\Phi_{state}(\mathbf{x}) = \frac{\sum_{j=1}^F \sum_{v=1}^V \sum_{n=1}^N \left| E_{inc}^{(v)}(\mathbf{r}_n; f_j) - \tilde{E}_{inc}^{(v)}(\mathbf{r}_n; f_j) \right|^2}{\sum_{j=1}^F \sum_{v=1}^V \sum_{n=1}^N \left| E_{inc}^{(v)}(\mathbf{r}_n; f_j) \right|^2} \quad (4)$$

$$\Phi_{data} = \frac{\sum_{j=1}^F \sum_{v=1}^V \sum_{m=1}^M \left| E_{scatt}^{(v)}(\mathbf{r}_m^{(v)}; f_j) - \tilde{E}_{scatt}^{(v)}(\mathbf{r}_m^{(v)}; f_j) \right|^2}{\sum_{j=1}^F \sum_{v=1}^V \sum_{m=1}^M \left| E_{scatt}^{(v)}(\mathbf{r}_m^{(v)}; f_j) \right|^2} \quad (5)$$

The unknowns of the inversion problem are

$$\mathbf{x} = \left\{ \tau(\mathbf{r}; f_{ref}); E_{tot}^{(v)}(\mathbf{r}_n; f_j) \right\} \quad n = 1, \dots, N; v = 1, \dots, V; j = 1, \dots, F. \quad (6)$$

The total number of unknowns for *MF*-based approaches is then given by

$$U_{MF} = 2N(1 + VF). \quad (7)$$

### 1.4 Reconstruction errors

The following integral error is defined

$$\Xi_{reg} = \frac{1}{N_{reg}} \sum_{n=1}^{N_{reg}} \frac{|\tau_n^{act} - \tau_n^{rec}|}{|\tau_n^{act} + 1|} \quad (8)$$

where *reg* indicates if the error computation covers

- the overall investigation domain ( $reg \Rightarrow tot$ ),
- the actual scatterer support ( $reg \Rightarrow int$ ),
- or the background region ( $reg \Rightarrow ext$ ).

## 2 Numerical Validation

### 2.1 Square-shaped object

#### 2.1.1 Parameters

##### Background

Inhomogeneous and nonmagnetic background composed by two half spaces

- Upper half space ( $y > 0$  - air):  $\epsilon_{ra} = 1.0$ ,  $\sigma_a = 0.0$ ;
- Lower half space ( $y < 0$  - soil):  $\epsilon_{rb} = 4.0$ ,  $\sigma_b = 10^{-3}$  [S/m];

##### Investigation domain ( $D_{inv}$ )

- Side:  $L_{D_{inv}} = 0.8$  [m];
- Barycenter:  $(x_{bar}^{D_{inv}}, y_{bar}^{D_{inv}}) = (0.00, -0.4)$  [m];

##### Time-Domain forward solver ( $FDTD$ - $GPRMax2D$ )

- Side of the simulated domain:  $L = 6$  [m];
- Number of cells:  $N^{FDTD} = 750 \times 750 = 5.625 \times 10^5$ ;
- Side of the  $FDTD$  cells  $l^{FDTD} = 0.008$  [m];
- Simulation time window:  $T^{FDTD} = 20 \times 10^{-9}$  [sec];
- Time step:  $\Delta t^{FDTD} = 1.89 \times 10^{-11}$  [sec];
- Number of time samples:  $N_t^{FDTD} = 1060$ ;
- Boundary conditions: perfectly matched layer ( $PML$ );
- Source type: Gaussian mono-cycle (first Gaussian pulse derivative, called “Ricker” in  $GPRMax2D$ )
  - Central frequency:  $f_0 = 300$  [MHz];
  - Source amplitude:  $A = 1.0$  [A];

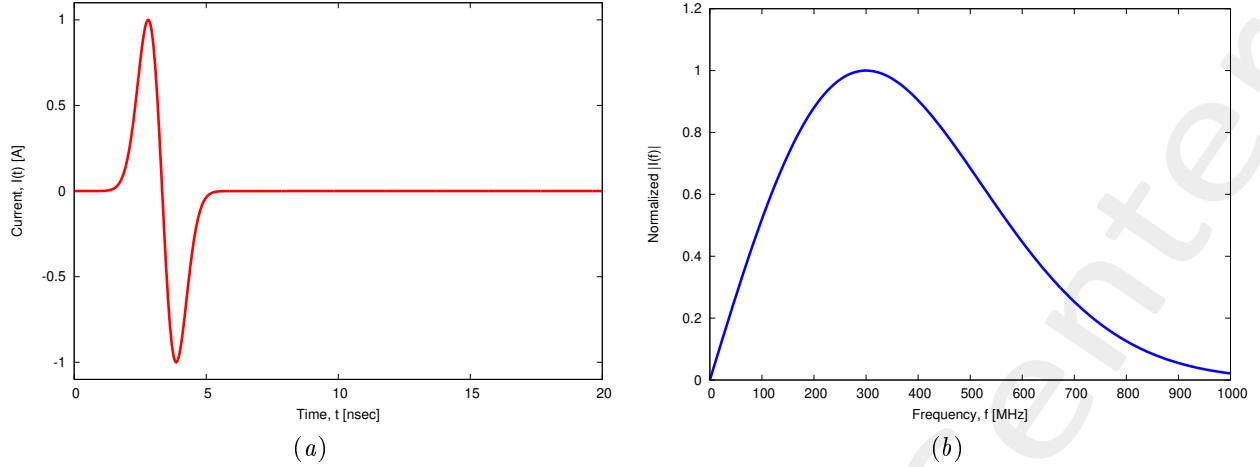


Figure 1: *GPRMax2D* excitation signal. (a) Time pulse, (b) normalized frequency spectrum.

### Frequency parameters

- Frequency range:  $f \in [f_{min}, f_{max}] = [200.0, 600.0]$  [MHz] ( $-3$  [dB] bandwidth of the Gaussian Monocycle excitation centered at  $f_0 = 300$  [MHz]);
- Frequency step:  $\Delta f = 100$  [MHz] ( $F = 5$  frequency steps in  $[f_{min}, f_{max}]$ );

$f$ [MHz]	$\lambda_a$ [m]	$\lambda_b$ [m]	$f^*$ [MHz]
200.0	1.50	0.75	200.5
300.0	1.00	0.50	297.6
400.0	0.75	0.37	401.1
500.0	0.60	0.30	498.1
600.0	0.50	0.25	601.6

Table 1: Considered frequencies and corresponding wavelength in the upper medium ( $\lambda_a$ , free space) and in the lower medium ( $\lambda_b$ , soil).  $f^*$  is the nearest frequency sample available from transformed time-domain data, and represents the real frequency considered by the inversion algorithm.

### Scatterer

- Type: square-shaped;
- Barycenter:  $(x_{obj}, y_{obj}) = (-0.08, -0.24)$  [m];
- Side:  $L_{obj,x} = L_{obj,y} = 0.16$  [m];
- Electromagnetic properties:  $\varepsilon_{r,obj} = 5.0$ ,  $\sigma_{obj} = 10^{-3}$  [S/m] ( $\sigma_{obj} = \sigma_b$ );
- Contrast function:  $\tau = 1.0 + j0.0$

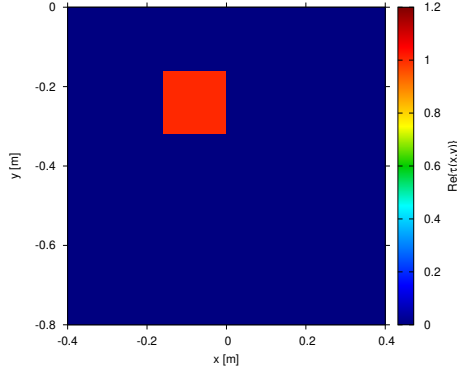


Figure 2: Actual object: offset square cylinder  $\tau = 1.0$ .

### Measurement setup

- Considered frequency:  $f_{min} = 200$  [MHz],  $\lambda_b = 0.75$  [m]. <sup>1</sup>
- $\#DoFs = 2ka = \frac{2\pi}{\lambda_b}L\sqrt{2} = \frac{2\pi}{0.75}0.8\sqrt{2} \simeq 9.5$ ;
- Number of views (sources):  $V = 10$ ;
  - $\min\{x_v\} = -0.5$  [m],  $\max\{x_v\} = 0.5$  [m];
  - height:  $y_v = 0.1$  [m],  $\forall v = 1, \dots, V$ ;
- Number of measurement points:  $M = 9$ ;
  - $\min\{x_m\} = -0.5$  [m],  $\max\{x_m\} = 0.5$  [m];
  - height:  $y_m = 0.1$  [m],  $\forall m = 1, \dots, M$ ;

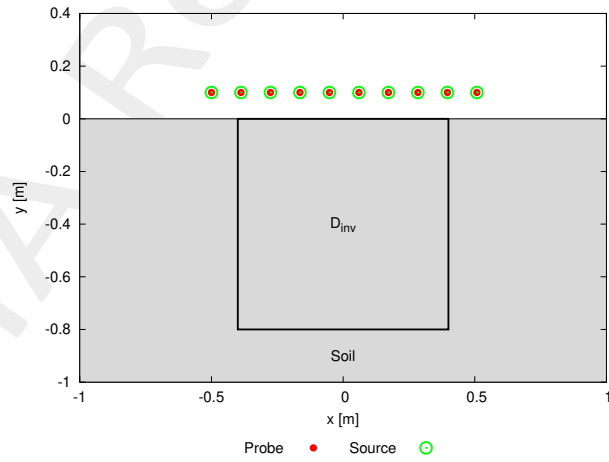


Figure 3: Location of the measurement points ( $M = 9$ ) and of the sources ( $V = 10$ ). Only one source is active for each view.

### Inverse solver parameters

- Shared parameters

<sup>1</sup>NOTE: This choice is done in order to keep the number of unknowns lower than 5000.

- Number of unknowns:  $U = 2N(1 + VF) = 4998$ ;
- Weight of the state term of the functional: 1.0;
- Weight of the data term of the functional: 1.0;
- Weight of the penalty term of the functional: 0.0;
- Convergence threshold:  $10^{-10}$ ;
- Variable ranges:

$$* \varepsilon_r \in [4.0, 5.2], \sigma \in [8.0 \times 10^{-4}, 1.2 \times 10^{-3}] [\text{S/m}];$$

$$* \Re\{E_{tot}^{int}\} \in [-8, 8], \Im\{E_{tot}^{int}\} \in [-8, 8];$$

- Degrees of freedom:

$$* \text{ Considered frequency: } f_{min} = 200 \text{ [MHz]}, \lambda_b = 0.75 \text{ [m]};$$

$$* \frac{(2ka)^2}{2} = \frac{\left(2 \times \frac{2\pi}{\lambda_b} \times \frac{L\sqrt{2}}{2}\right)^2}{2} = 4\pi^2 \left(\frac{L}{\lambda_b}\right)^2 = 4\pi^2 \left(\frac{0.8}{0.75}\right)^2 \simeq 44.87;$$

- Number of cells:  $N = 49 = 7 \times 7$ ;
- Maximum number of *IMSA* steps:  $S = 6$ ;
- Side ratio threshold:  $\eta_{th} = 0.2$ ;

- ***MF – IMSA – PSO* parameters**

- Maximum number of iterations:  $I = 20000$ ;
- Swarm dimension:  $P = \frac{5}{100} \times U = 250$ ;
- $C_1 = C_2 = 2.0$ ;
- Inertial weight:  $w = 0.4$ ;
- Velocity clamping: enabled;

- ***FH – IMSA – PSO* parameters**

- Maximum number of iterations:  $I = 20000$ ;
- Swarm dimension:  $P = 250$  (to keep the same parameters used for *MF – IMSA – PSO*);
- $C_1 = C_2 = 2.0$ ;
- Inertial weight:  $w = 0.4$ ;
- Velocity clamping: enabled;

- ***MF – IMSA – CG* parameters**

- Maximum number of iterations:  $I = 200$ ;

- ***FH – IMSA – CG* parameters**

- Maximum number of iterations:  $I = 400$  ;

### Signal to noise ratio (on $E_{tot}(t)$ )

- $SNR = \{50, 40, 30, 20\}$  [dB] ;

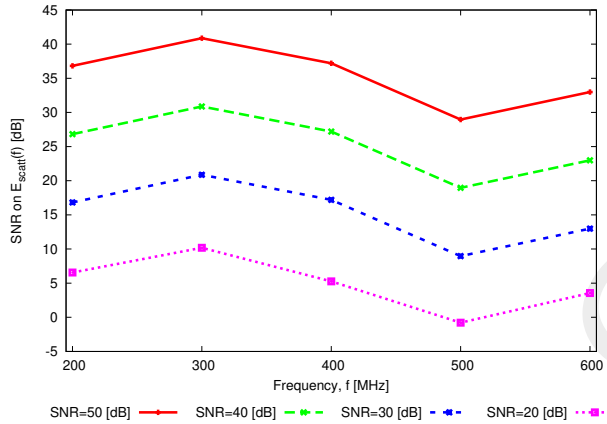


Figure 4: Signal to noise ratio ( $SNR$  [dB]) computed on the external scattered field in frequency domain for each considered frequency and for each input  $SNR$  on the measured total field in time-domain.

SNR on $E_{tot}(t)$ [dB]	Av. SNR on $E_{scatt}(f)$ [dB]
50	35
40	25
30	15
20	5

Table 2: Average  $SNR$  measured on the scattered field in frequency domain.

**2.1.2  $MF - IMSA - PSO$  vs.  $MF - IMSA - CG$  vs.  $FH - IMSA - PSO$  vs.  $FH - IMSA - CG$ : Final reconstructions**

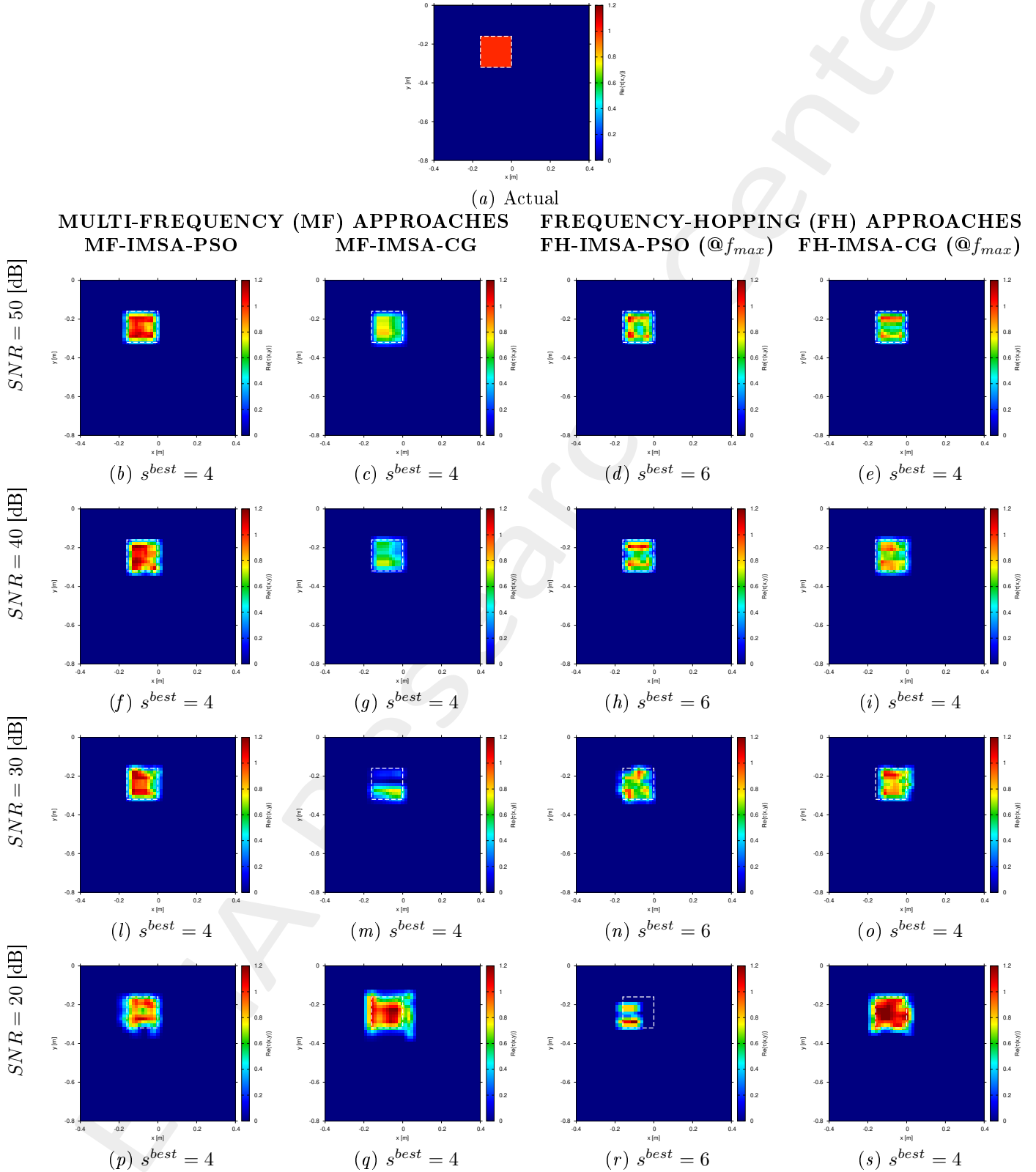


Figure 5:  $MF - IMSA - PSO$  vs.  $MF - IMSA - CG$  vs.  $FH - IMSA - PSO$  vs.  $FH - IMSA - CG$ : Retrieved dielectric profiles at the  $IMSA$  convergence step ( $s^{best}$ ).

### 2.1.3 $MF - IMSA - PSO$ : Intermediate reconstructions

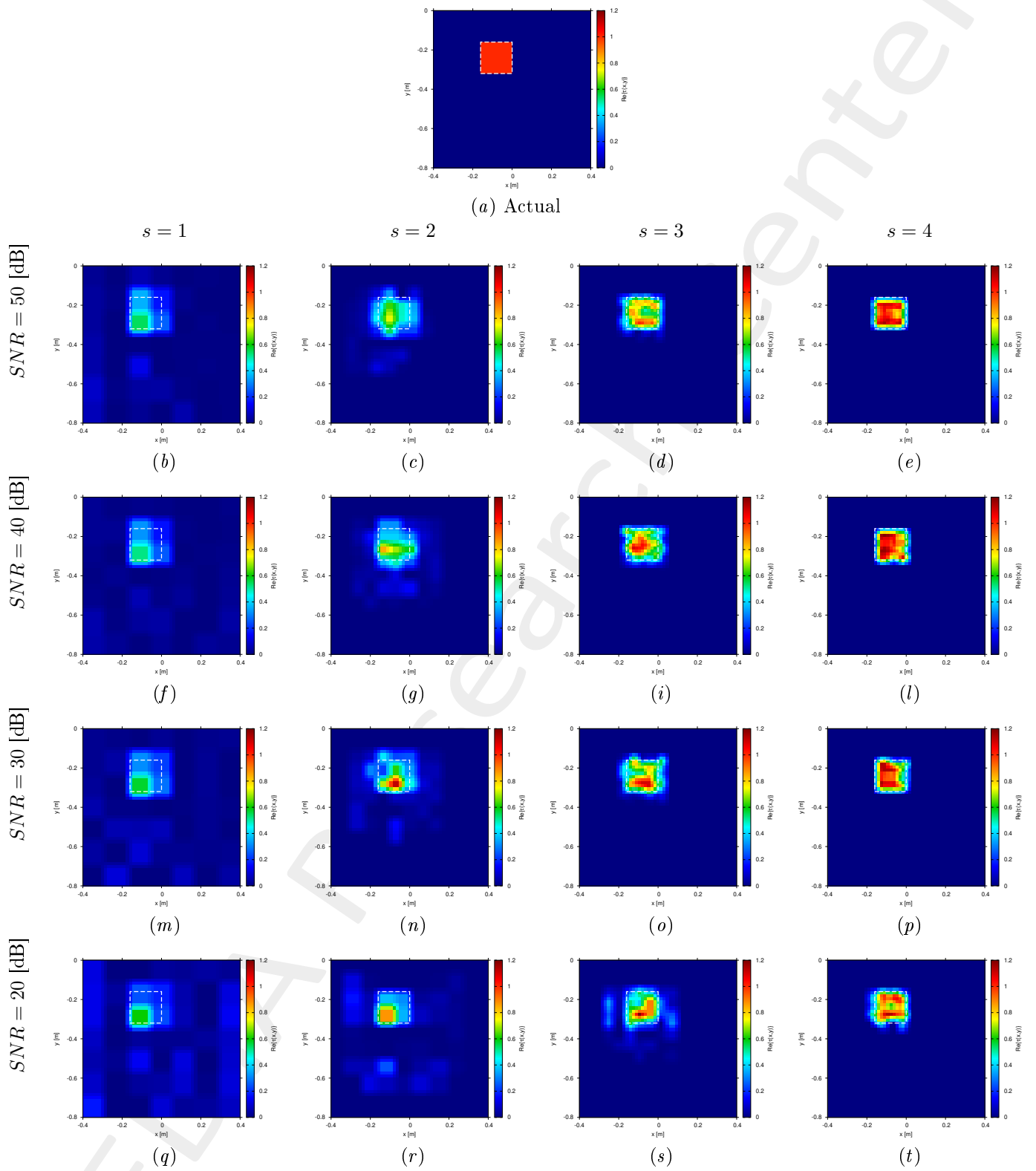


Figure 6:  $MF - IMSA - PSO$ : Retrieved dielectric profiles at each  $IMSA$  step.

#### 2.1.4 $MF - IMSA - CG$ : Intermediate reconstructions

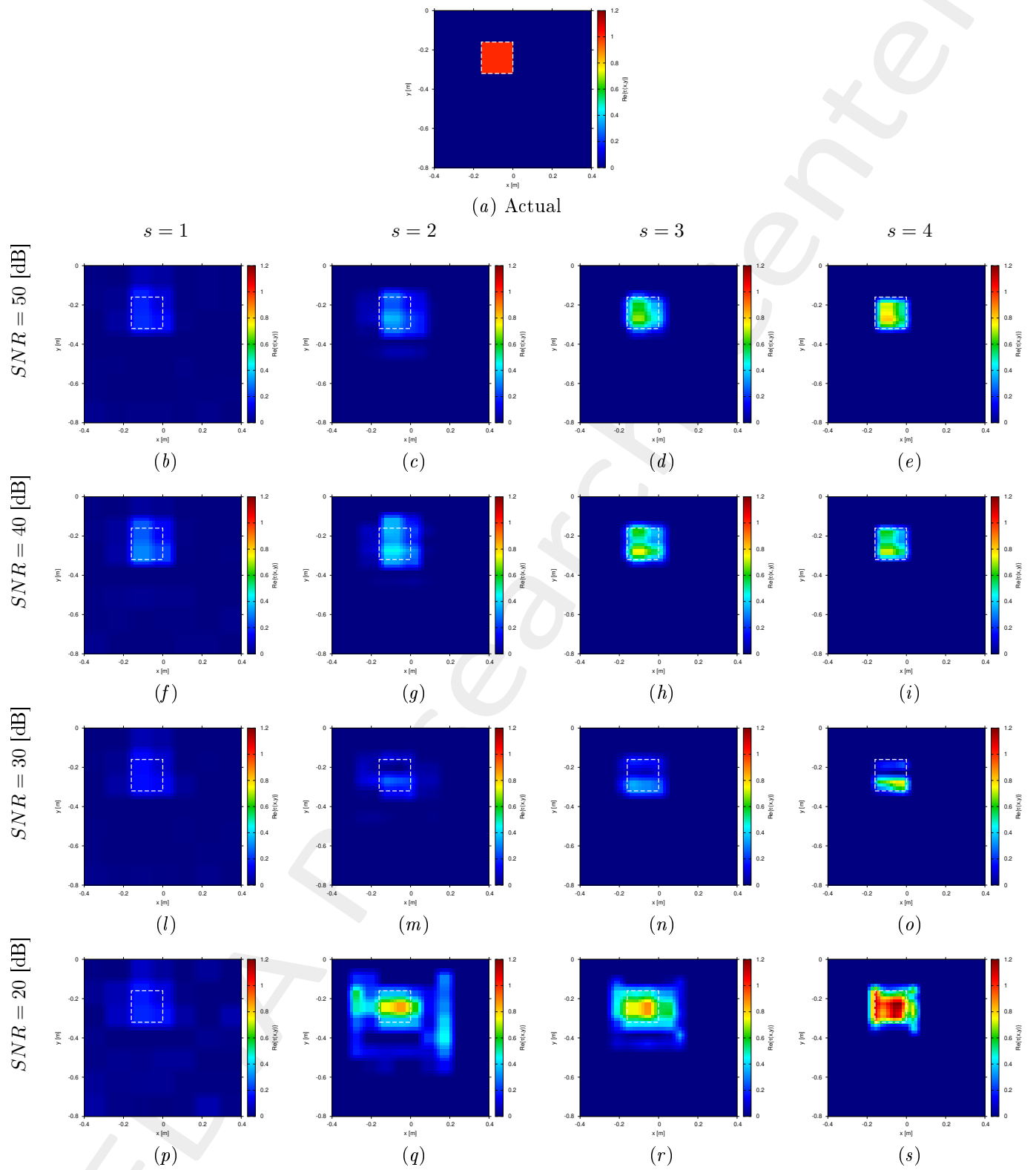


Figure 7:  $MF - IMSA - CG$ : Retrieved dielectric profiles at each  $IMSA$  step.

### 2.1.5 Reconstruction errors

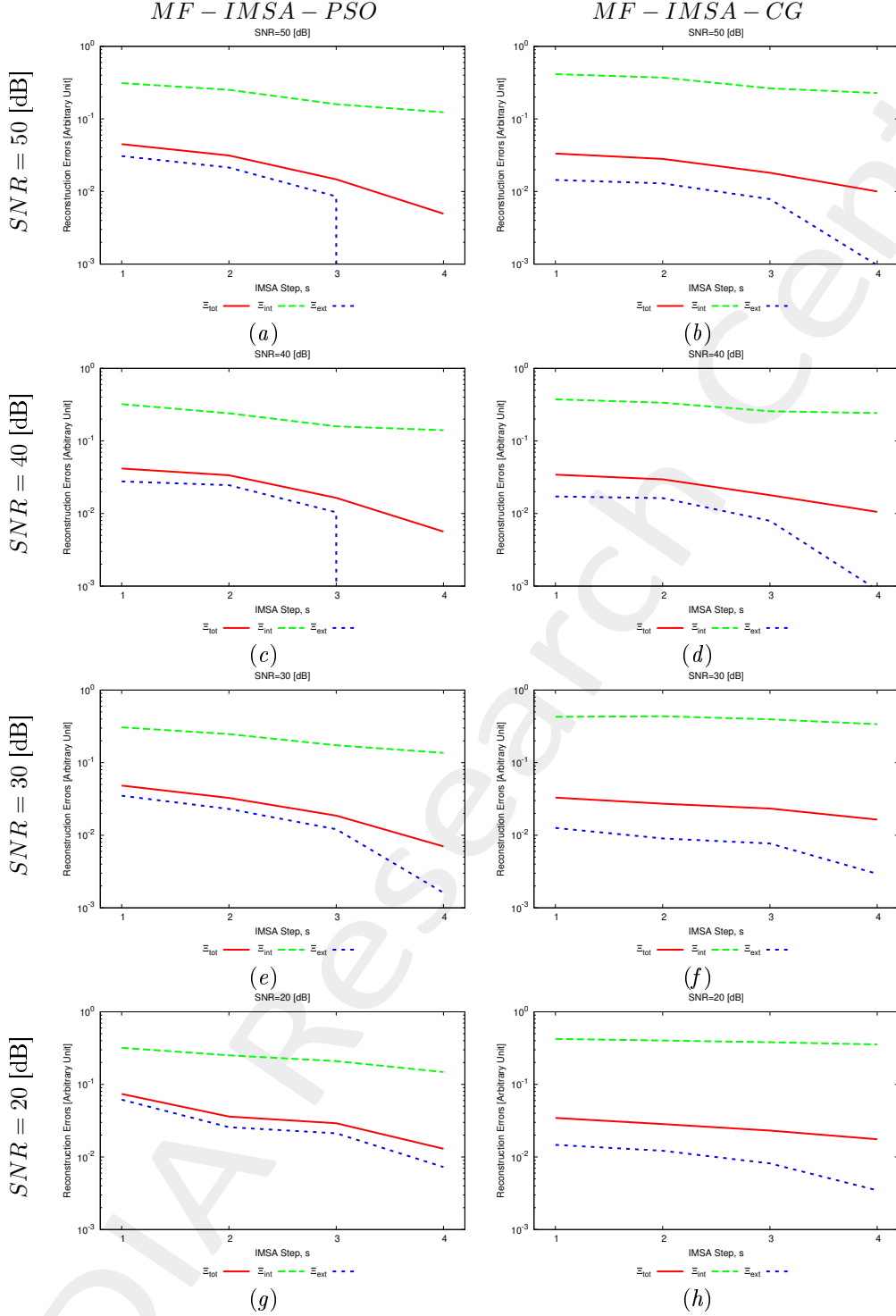


Figure 8:  $MF - IMSA - PSO$  vs.  $MF - IMSA - CG$ : Reconstruction error evolution.

### 2.1.6 Evolution of the cost function

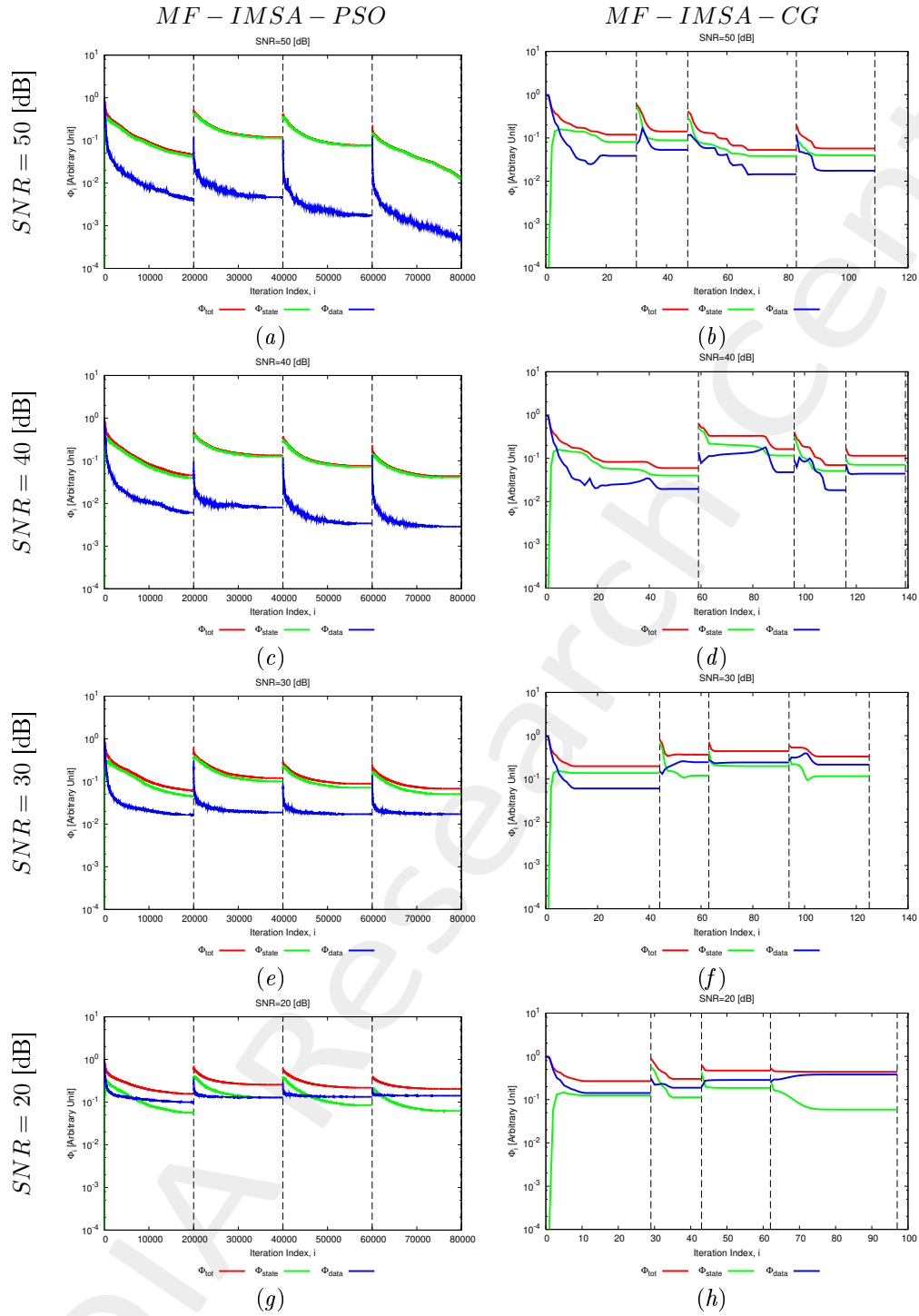


Figure 9:  $MF - IMSA - PSO$  vs.  $MF - IMSA - CG$ : Evolution of the cost function.

## 2.2 Conclusions

The reported results indicate that

- The proposed  $MF - IMSA - PSO$  method overcomes its deterministic counterpart ( $MF - IMSA - CG$ ), that is based on a Conjugate Gradient ( $CG$ ) solver [5];
- The superior performances of the  $MF - IMSA - PSO$  over the  $MF - IMSA - CG$  are due to the exploitation of the  $PSO$  solver, that is a global optimization technique [1];
- The  $MF - IMSA - PSO$  is able to provide better reconstructions also with respect to frequency-hopping ( $FH$ )-based approaches such as the  $FH - IMSA - PSO$  and the  $FH - IMSA - CG$  [3].

---

**More information on the topics of this document can be found in the following list of references.**

## References

- [1] P. Rocca, M. Benedetti, M. Donelli, D. Franceschini, and A. Massa, “Evolutionary optimization as applied to inverse scattering problems,” *Inverse Probl.*, vol. 25, no. 12, pp. 1-41, 2009 (DOI: 10.1088/0266-5611/25/12/123003).
- [2] P. Rocca, G. Oliveri, and A. Massa, “Differential Evolution as applied to electromagnetics,” *IEEE Antennas Propag. Mag.*, vol. 53, no. 1, pp. 38-49, Feb. 2011 (DOI: 10.1109/MAP.2011.5773566).
- [3] M. Salucci, G. Oliveri, and A. Massa, “GPR prospecting through an inverse scattering frequency-hopping multi-focusing approach,” *IEEE Trans. Geosci. Remote Sens.*, vol. 53, no. 12, pp. 6573-6592, Dec. 2015 (DOI: 10.1109/TGRS.2015.2444391).
- [4] M. Salucci, L. Poli, and A. Massa, “Advanced multi-frequency GPR data processing for non-linear deterministic imaging,” *Signal Processing - Special Issue on 'Advanced Ground-Penetrating Radar Signal-Processing Techniques'*, vol. 132, pp. 306-318, Mar. 2017 (DOI: 10.1016/j.sigpro.2016.06.019).
- [5] M. Salucci, L. Poli, N. Anselmi and A. Massa, “Multifrequency particle swarm optimization for enhanced multiresolution GPR microwave imaging,” *IEEE Trans. Geosci. Remote Sens.*, vol. 55, no. 3, pp. 1305-1317, Mar. 2017 (DOI: 10.1109/TGRS.2016.2622061).
- [6] A. Massa, P. Rocca, and G. Oliveri, “Compressive sensing in electromagnetics - A review,” *IEEE Antennas Propag. Mag.*, pp. 224-238, vol. 57, no. 1, Feb. 2015 (DOI: 10.1109/MAP.2015.2397092).
- [7] A. Massa and F. Texeira, “Guest-Editorial: Special Cluster on Compressive Sensing as Applied to Electromagnetics,” *IEEE Antennas Wireless Propag. Lett.*, vol. 14, pp. 1022-1026, 2015 (DOI: 10.1109/LAWP.2015.2425011).
- [8] N. Anselmi, G. Oliveri, M. Salucci, and A. Massa, “Wavelet-based compressive imaging of sparse targets,” *IEEE Trans. Antennas Propag.*, vol. 63, no. 11, pp. 4889-4900, Nov. 2015 (DOI: 10.1109/TAP.2015.2444423).
- [9] G. Oliveri, N. Anselmi, and A. Massa, “Compressive sensing imaging of non-sparse 2D scatterers by a total-variation approach within the Born approximation,” *IEEE Trans. Antennas Propag.*, vol. 62, no. 10, pp. 5157-5170, Oct. 2014 (DOI: 10.1109/TAP.2014.2344673).
- [10] T. Moriyama, G. Oliveri, M. Salucci, and T. Takenaka, “A multi-scaling forward-backward time-stepping method for microwave imaging,” *IEICE Electron. Expr.*, vol. 11, no. 16, pp. 1-12, Aug. 2014 (DOI: 10.1587/elex.11.20140578).
- [11] T. Moriyama, M. Salucci, M. Tanaka, and T. Takenaka, “Image reconstruction from total electric field data with no information on the incident field,” *J. Electromagnet. Wave.*, vol. 30, no. 9, pp. 1162-1170, 2016 (DOI: 10.1080/09205071.2016.1182876).
- [12] F. Viani, L. Poli, G. Oliveri, F. Robol, and A. Massa, “Sparse scatterers imaging through approximated multi-task compressive sensing strategies,” *Microw. Opt. Technol. Lett.*, vol. 55, no. 7, pp. 1553-1557, Jul. 2013 (DOI: 10.1002/mop.27612).

- 
- [13] M. Salucci, N. Anselmi, G. Oliveri, P. Calmon, R. Miorelli, C. Reboud, and A. Massa, "Real-time NDT-NDE through an innovative adaptive partial least squares SVR inversion approach," *IEEE Trans. Geosci. Remote Sens.*, vol. 54, no. 11, pp. 6818-6832, Nov. 2016 (DOI: 10.1109/TGRS.2016.2591439).
  - [14] L. Poli, G. Oliveri, and A. Massa, "Imaging sparse metallic cylinders through a local shape function bayesian compressing sensing approach," *J. Opt. Soc. Am. A*, vol. 30, no. 6, pp. 1261-1272, Jun. 2013 (DOI: 10.1364/JOSAA.30.001261).
  - [15] M. Donelli, D. Franceschini, P. Rocca and A. Massa, "Three-dimensional microwave imaging problems solved through an efficient multiscaling particle swarm optimization," *IEEE Trans. Geosci. Remote Sens.*, vol. 47, no. 5, pp. 1467-1481, May 2009 (DOI: 10.1109/TGRS.2008.2005529).